Radar Detection Performance Prediction using Measured UAVs RCS Data

Massimo Rosamilia, *Student Member, IEEE*, Alessio Balleri, Antonio De Maio, *Fellow, IEEE*, Augusto Aubry, *Senior Member, IEEE*, and Vincenzo Carotenuto, *Senior Member, IEEE*

Abstract—This paper presents measurements of Radar Cross Section (RCS) of five Unmanned Aerial Vehicles (UAVs), comprising both consumer grade and professional small drones, collected in a semi-controlled environment as a function of azimuth aspect angle, polarization and frequency in the range 8.2-18 GHz. The experimental setup and the data pre-processing, which include coherent background subtraction and range gating procedures, are illustrated in detail. Furthermore, a thorough description of the calibration process, which is based on the substitution method, is discussed. Then, a first-order statistical analysis of the measured RCSs is provided by means of the Cramér–von Mises (CVM) distance and the Kolmogorov–Smirnov (KS) test. Finally, radar detection performance is assessed on both measured and bespoke simulated data (leveraging the results of the developed statistical analysis), including, as benchmark terms, the curves for non-fluctuating and Rayleigh fluctuating targets.

Index Terms—Radar Cross Section, Measured Data, Statistical Analysis, Radar Detection Performance, Drone Detection.

I. INTRODUCTION

The detection of small Unmanned Aerial Vehicles (UAVs), commonly referred to as drones, is a challenging problem in both civilian and defence applications. This is due to the unsuitability of many current surveillance radars to provide adequate detection performance for such types of targets, characterized by weak radar signatures, low flight altitude and slow speed. Remarkably, the detection of UAVs is also problematic due to the high number of false alarms resulting from the similarity between radar signatures of drones and birds (see [3], [4]). On the other hand, the cyber and physical threats from drones is becoming a serious issue [5] due to the exponential increase in the use of small commercial drones (see [6] for an overview of threats from unauthorized small commercial UAVs). In this context, collecting drone data and analyzing their Radar Cross Section (RCS) is a critical step towards the design of appropriate system architectures capable of dealing with these types of targets as well as for the development of an accurate performance prediction of existing algorithms.

Not surprisingly, some valuable experimental campaigns aimed at characterizing UAV radar signatures have been conducted and the corresponding results are available in the open literature. In [7], the RCS of small UAVs have been measured for different aspect angles in the frequency interval $8 - 12$ GHz and in VV polarization. The measurements have also been examined using the Inverse Synthetic Aperture Radar (ISAR) method, which provides useful information regarding the components that mostly contribute to the drone signature. Similarly, ISAR imaging has been also employed in [8] to analyze the RCS of several small consumer drones measured in the frequency bands $3 - 6$ GHz and $12 - 15$ GHz for different aspect angles. In [9], six commercial UAVs have been measured at 15 GHz and 25 GHz for both HH and VV polarizations. The RCS measurements of two off-the-shelf drones in the frequency band $5.8 - 8.2$ GHz has been addressed in [10], and in [11] RCS data of several drones have been collected in the frequency range $26 - 40$ GHz. In [12] the RCS measurement of small UAVs has been investigated in challenging scenarios (outdoor environments, hangars, etc.) using a portable system. Some measurements in the Ku radar band have been conducted in [13], whereas, unlike aforementioned references, [14] has presented three-dimensional RCS measurements of a nano-drone from 23 GHz to 25 GHz. Simulation and experimental results of micro-drone rotor blade electromagnetic scattering as a function of polarization, frequency and azimuth angle have been presented in [15], whereas a highly accurate UAV RCS simulation has been developed in [16] and the corresponding results compared with those of measurements and simpler simulation approaches. In [17], the RCSs of some nano and micro drones have been collected in the X-band for several elevation angles, and some statistics related to measured RCS data have been provided. A statistical analysis of experimental data of nine flying drones, collected with a Frequency-Modulated Continuous Wave (FMCW) Ku-band radar has been presented in [18], with emphasis on the analysis of amplitude fluctuations of the drone body/blades as well as the signature decorrelation time. Besides, [9] has presented both a statistical analysis of the measured RCS and a performance prediction of a specific UAV recognition system, whereas in [13] radar detection performance has been analyzed in the context of a short-range battlefield radar. Further study on UAV RCS-based recognition using statistical-based parameters, machine learning, and deep learning techniques has been presented

in [19]. In [20], an experimental 35 GHz FMCW coherent radar has been proposed to detect small UAVs, whilst [21] has investigated the detection of drones using the MIRA-CLE Ka system, which is a MIMO radar developed for imaging applications. In [22], the detection and the RCS measurement of a DJI-Phantom 4 have been assessed with the RAD-DAR, which is an experimental FMCW coherent radar operating at X-band. Detection and tracking using the multistatic Netted Radar (NetRAD) system have been addressed in [23] leveraging micro-Doppler analysis to discriminate flying drones from clutter returns, whereas discussions on UAV detection via FMCW radars have been also provided in [24], [25]. Furthermore, [26] has provided an overview of the state of the art in drone activity monitoring using radar systems, and in [6] particular emphasis has been placed on the current detection and tracking techniques tailored to drone threats based on radars, acoustic and other available sensors.

Although some statistical analyses of the RCS of drones collected at several frequencies have been reported in [9]–[11], [14], this paper presents an extensive statistical analysis of the RCS of five drones measured in the whole X- and Ku-band, HH and VV polarization, for different azimuth aspect angles using an angular resolution of 0.1 degree and a frequency resolution of 1.5 MHz. In addition, unlike the mentioned papers whose focus is on drone classification, the main purpose of this study is the assessment of search radar performance on measured data, with UAVs modeled as point-like objects. The scope of this paper is twofold: presenting the statistical analysis of the RCS signatures of five drones, i.e., AscTec Firefly, AscTec Pelican, Venom VN10, Parrot AR.DRONE, and DJI Matrice 100, and evaluating the radar detection performance using both measured RCSs and tailored fluctuation models, i.e., fitting UAV RCS data. To this end, the raw RCS data are collected in a semi-controlled environment as a function of frequency, azimuth aspect angle and polarization in the interval $8.2 - 18$ GHz. A complete description of the experimental setup and the data pre-processing, from signal acquisition to the calibrated RCS measurements, is provided. Specifically, the pre-processing operations, which include Coherent Background Subtraction (CBS) and range gating procedures, are illustrated with a discussion on the RCS calibration procedure relying on the substitution method. Moreover, the accuracy of the measurements, mainly affected by noise-induced uncertainties, is investigated in terms of the acquisitions Signal to Noise Ratio (SNR). The results are analyzed considering sliding frequency intervals of 200 MHz corresponding to a range resolution of 0.75 m, which allows to model the drones as point-like targets. Furthermore, a detailed first-order statistical analysis of the measured drone RCSs is performed by fitting the data with (one- and two-parameters) distributions typically employed to model RCS fluctuations [27], via the minimization of the Cramér–von Mises (CVM) distance between the empirical and the theoretical Cumulative Distribution Functions (CDFs). The Kolmogorov–Smirnov (KS) test is also employed to further study the goodness-of-fit of the chosen distribution. Hence, in the context of a coherent detection, radar performance is studied versus the integrated SNR at the radar receiver, with the drones
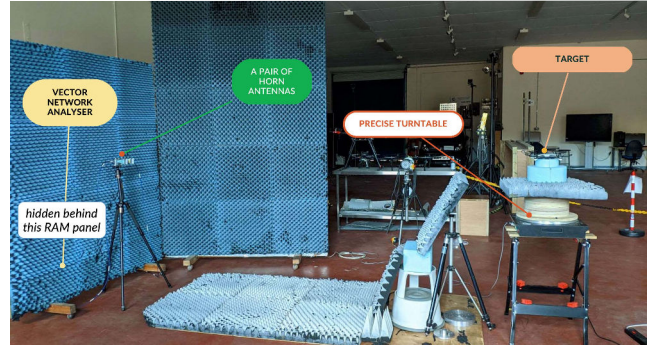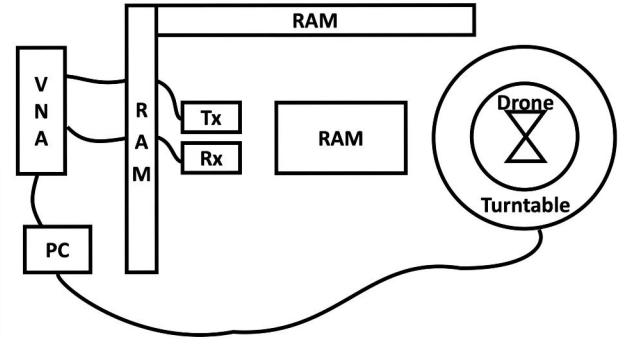

Fig. 1. A notional representation and an actual snapshot of the experimental setup.

RCS modeled as a fluctuating target from Coherent Processing Interval (CPI) to CPI. In particular, the detection performance, evaluated leveraging both measured and simulated fluctuations (according to the inferred distribution), is compared with standard benchmark based on stationary (Swerling 0) and random (Swerling 1) targets.

The rest of the paper is organized as follows. Section II presents the experimental setup and describes the pre-processing steps. The statistical behavior of the measured RCSs is analyzed in Section III, while the radar detection performance is evaluated in Section IV. Finally, Section V addresses concluding remarks and outlines some possible future research avenues.

II. EXPERIMENTAL SETUP

In this section, a thorough description of the experimental setup involved in the measurement campaign is provided along with details on data pre-processing, measurements uncertainties and calibration. The RCS data has been collected in a laboratory environment using the measurement setup depicted in Fig. 1 which is composed of

- Radar Absorbing Material (RAM) panels to mitigate multipath reflections from the ceiling, walls and floor;
- a 2-port MS46322A Anritsu Vector Network Analyzer (VNA) capable of providing a dynamic range greater than 100 dB up to 40 GHz. By transmitting a stepped-frequency waveform, the VNA measures the frequency response of the illuminated area over a pre-defined bandwidth using at most $N_f = 16001$ frequencies in the probing waveform. The VNA is controlled remotely from a PC using an Ethernet cable;

- a LinearX precision turntable with an angular step resolution of (up to) 0.1 degrees. The turntable is fully controlled remotely from a PC through commands sent via an RS-232 serial connection;
- a standard PC to control and synchronize the turntable and the VNA via the Laboratory Virtual Instrument Engineering Workbench (LabVIEW) as well as to store the raw data. The PC is also used to process the data offline;
- a pair of identical standard horn antennas, one for transmission and the other for reception; they are connected to the two ports of the VNA by means of low-loss coaxial cables and co-located on a tripod. The positions of the antennas have been adjusted with a cross-laser level to steer the antenna boresights at the target. Rotating the antennas allowed data collection for different polarizations.

Before proceeding with the measurements, the VNA has been calibrated using the standard "thru" calibration procedure to provide a measurement setup with a flat frequency response up to the antennas. The LabVIEW scripts have been designed to trigger a turntable step rotation after the data acquisition by the VNA at a specific aspect angle. This has guaranteed collections of frequency responses with a stationary target. In particular, a short time delay has been also included before collecting a new measurement to ensure that the setup was actually stationary after each step rotation.

Although the VNA measured all S-parameters [28] at each frequency, for the considered experiments only the forward complex transmission coefficient S_{21}, corresponding (for the case at hand) to the spectral response of the illuminated area at a given frequency, has been recorded and analyzed. The HH-pol and VV-pol returns from five drones have been measured versus frequency and target azimuth aspect angle using two different pairs of horn antennas. Specifically, measurements in the interval $7 - 13$ GHz are collected via Marconi Instruments model 6036/4 antennas, operating from 8.2 GHz to 12.4 GHz. Besides, data at the Ku-bands ($12 - 18$ GHz) are acquired via Narda, model 639 antennas, operating from 12.4 GHz to 18 GHz[1]. Regardless of the employed antennas, the VNA has been configured to sample the 6 GHz bandwidth with $N_f = 4001$ frequency points and the turntable azimuth step resolution has been set to 0.1 degrees for 360 degree rotations. For measurements in the range $7 - 13$ GHz, the distance between the antennas and the target has been set to approximately 7.2 m, whilst for the higher frequency bandwidth a distance of approximately 3.4 m has been used. A summary of the experimental parameters used to collect and analyze the data is reported in Table I, whereas the specifications of the analyzed drones are listed in Table II. Note that the employed measurement setup falls in the so-called near-

TABLE I
SETUP AND ACQUISITION PARAMETERS.

Parameter	Setup 1	Setup 2
Frequency Interval	$7 - 13$ GHz	$12 - 18$ GHz
Analyzed Frequency Bandwidth	$8.2 - 12.4$ GHz	$12.4 - 18$ GHz
Bandwidth B	6 GHz	6 GHz
Azimuth Rotation Step	0.1 degrees	0.1 degrees
Frequency Steps N_f	4001	4001
Frequency Stepsize Δf	1.5 MHz	1.5 MHz
Unambiguous Range	99.93 m	99.93 m
Target-antennas Distance	≈ 7.2 m	≈ 3.4 m
Distance from Ceiling	2.71 m	2.71 m
Height above Floor	1.28 m	1.28 m
Range Gating	$6.5 - 7.8$ m	$1.5 - 4.6$ m
Number of FFT/IFFT Points	400100	400100

field[2] non-anechoic range scenario [29]. Before concluding this section, a discussion on data pre-processing (including CBS, range gating, and frequency windowing) together with the RCS calibration process follows.

A. Data Pre-processing

For each acquisition, a background measurement (obtained in the absence of the drone) has been collected and subtracted coherently in the frequency domain from all the data acquired in the presence of the target. Range-gating has been then applied to the high range resolution background-free profile to further isolate the target response in range from residual multipath reflections which could not be eliminated with the CBS [29], [30]. To achieve this, a tailored rectangular window, with parameters matched to the drone size and the target-antennas distance (see Table I), has been used. Fig. 2 illustrates an example of the range gating procedure performed for a measurement in the interval $7 - 13$ GHz. As a matter of fact, the clean signal is obtained as the product of the target range profile and a rectangular window, defined as 1 within the swath $6.5 - 7.8$ m and 0 elsewhere. The figure clearly shows that the entire target response is located within the considered window, however outside that region a multipath contribution (due likely to the ceiling) is present at 8.4 m. Furthermore, strong interference is also evident at approximately 9.8 m due reasonably to the absence of overall back-wall scattering when the drone is present (a phenomenon known as "shadowing"), which nullifies the effect of the CBS on that specific range.

The frequency spectrum of the clean signatures has been then used to extract the point-like target response over a moving bandwidth of 200 MHz, corresponding to a range resolution of 0.75 m. Precisely, the frequency domain is discretized in several frequency bins of 200 MHz having central frequencies $\{8.3 \text{ GHz} + (i \times 100) \text{ MHz}, i = 0, \ldots, 96\}$ and the data are processed separately in each of them. Therein, the target can be approximated as a point-like reflector (i.e., target scatterers within the range resolution cell) whose power

---

[1]Due to the frequency response characteristics of the antennas employed in the two measurement setups, the data acquired outside the spectrum portions $8.2 - 12.4$ GHz, for the first setup, and $12.4 - 18$ GHz, for the second setup, have been discarded.

[2]Since the measurements have been collected in the near-field region, the resulting RCS values can exhibit some deviations from the actual ones. However, it is worth pointing out that the provided results are aligned with those obtained in previous far-field measurement campaign, when comparisons are possible, thus supporting the reliability of the conducted assessment.

TABLE II
MEASURED DRONES SPECIFICATIONS.

| Drone	# Rotors	Blades Size	Weight	Width	Depth	Height	Primary Use
AscTec Firefly	6	210 mm	1600 g	470 mm	430 mm	165 mm	Mapping/Surveying
AscTec Pelican	4	250 mm	1650 g	360 mm	360 mm	188 mm	Film & Photo/Mapping/Surveying
Venom VN10	4	135 mm	148 g	290 mm	210 mm	38 mm	Film & Photo
Parrot AR.DRONE 2.0	4	190 mm	420 g	517 mm	517 mm	127 mm	Film & Photo
DJI Matrice 100	4	345 mm	2355 g	759 mm	755 mm	205 mm	Film & Photo/Mapping/Surveying
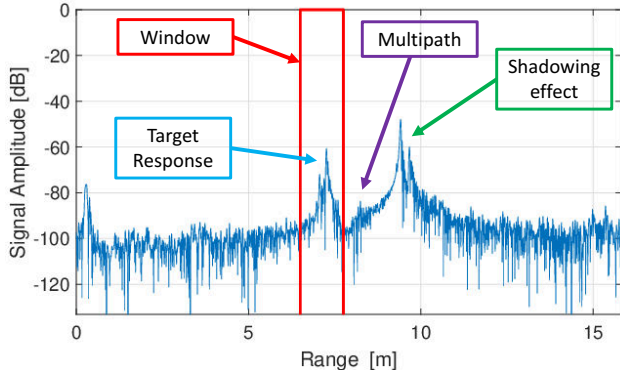
Fig. 2. Representation of the range gating procedure in the range/time domain. The range gating is performed by means of a rectangular window (displayed as a solid red line).

response (i.e., non-calibrated RCS) is extracted as the squared magnitude peak in the time domain.

B. RCS Measurements and Calibration

For a given target measurement, after the pre-processing stage (comprising CBS, range gating and frequency band selection) the resulting squared magnitude peak value in the range domain constitutes the power of the target return and is theoretically related to its RCS for the analyzed frequency bin via the radar equation. However, in the process of measuring the absolute RCS of a particular target, it is essential to include an accurate RCS calibration step. The substitution method [29] is the most often used calibration procedure for RCS measurements, which involves measuring a calibrating target (with a known RCS) with the same test-bed used to collect data from the target under test [29]. As a result, each measurement related to the RCS of the calibrating target at a given frequency[3] is compared with the theoretical RCS, and the resulting dB difference is utilized to calibrate the target measurements, provided that the test-bed, as well as the system parameters, are stationary. To this end, conductive spheres are the most commonly used calibrating targets, not only because their response does not change with aspect angle and polarization, but also because the RCS of such objects (assumed ideally manufactured) can be determined analytically [31], [32].

[3] The peak power of the calibrating target is measured as the squared magnitude peak in the time domain of the received response after CBS, range gating, and pass-band filtering around the considered frequency bin.

Precisely, the calibration factor for a given frequency bin with central frequency f and polarization p is determined as

$$K(f,p) = \frac{\sigma_{sph}(f,p)}{\sigma_{th,sph}(f)}, \ p = \{HH, VV\} \tag{1}$$

where $\sigma_{sph}(f,p)$ is the measurement of the received peak power of the sphere for the considered polarization p and analyzed frequency bin f, whereas $\sigma_{th,sph}(f)$ is the theoretical RCS at the central frequency f. As a consequence, the calibrated RCS of a target can be computed as

$$\hat{\sigma}(f,\theta,p) = \frac{\sigma_{tg}(f,\theta,p)}{K(f,p)} \tag{2}$$

where $\sigma_{tg}(f,\theta,p)$ is the measurement of the peak power return of the object under test, with reference to the angle θ, polarization p, and frequency bin centered at f.

The technique employed to measure the RCS of the drones in a specific polarization is summarized in **Procedure 1**.

In the performed campaign, a conductive 10 cm diameter sphere has been used to calibrate the drone measurement data. To assess the measurement accuracy of the collected RCS (after the calibration procedure), three independent measurements of the same sphere have been taken, with the first serving as a reference (to compute the calibration factors) and the others as tests (to validate the calibration procedure). As a matter of fact, measuring the error of the difference between the known and the measured RCS is a simple and effective way to estimate the overall uncertainty connected to the experimental setup at hand [29]. The results reported in Fig. 3 show that, as expected, the calibrated RCS of the first measurement achieves the theoretical one, while those related to the test measurements exhibit a mismatch less than 1.4 dB in the $8.2 - 12.4$ GHz range and less than 0.5 dB in the $12.4 - 18$ GHz bandwidth.

In this regard, the errors between the calibrated tests data (measurements 2 and 3) and the theoretical values are mainly due, as illustrated below, to the SNR of the measured data which, varies from 11 to 24 dB for the first range of frequencies and from 19 to 30 dB for the other one. The SNR of the measured data is computed in the time domain as the ratio between the peak power values of the target response (obtained as specified before) and the power of the strongest noise sample (computed performing gating on a range window not affected by the target presence, e.g., $20 - 30$ m). Hence, according to [29] and [33], under reasonable acquisition setups the uncertainty $\Delta\sigma$ (expressed in dB) associated with the
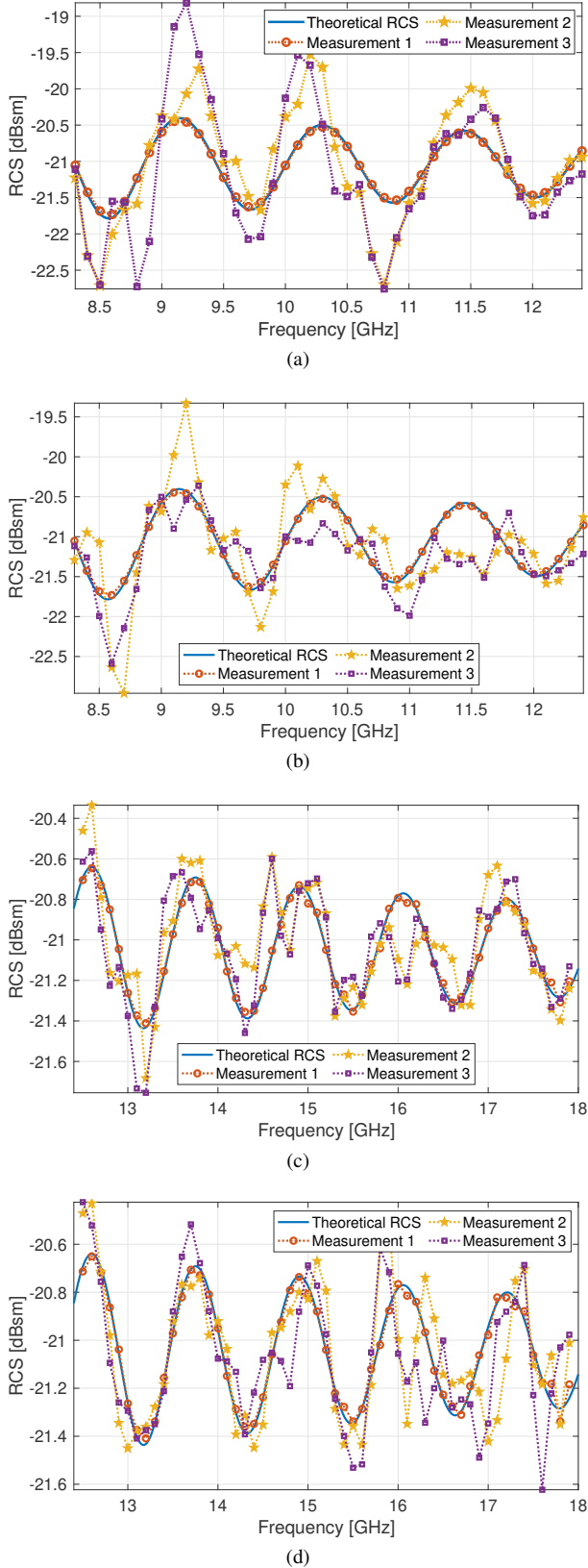
Fig. 3. Calibrated versus theoretical RCS of a conductive sphere with a diameter of 10 cm in the frequency interval: (a) and (b) 8.2-12.4 GHz, (c) and (d) 12.4-18 GHz. As to the polarization, (a) and (c) consider the HH case, whereas (b) and (d) refer to the VV setup. The calibration procedure exploits the first measurement.

Procedure 1 RCS measurement of a target as a function of frequency over different aspect angles for a given polarization.

Input raw data (with and without target) for a given polarization

1. load background data;
2. **for** $\theta \in \{i \times 0.1, i = 0, \ldots, 3599\}$
   2.A. load the data with target aspect angle θ and polarization p;
   2.B. perform CBS;
   2.C. apply range gating on target's range profile;
   2.D. **for** $f \in \{8.3 \text{ GHz} + (i \times 100) \text{ MHz}, i = 0, \ldots, 96\}$
     a) pass-band filter in the interval from $f - 100$ MHz to $f + 100$ MHz;
     b) estimate the target power return $\sigma_{tg}(f, \theta, p)$ as the squared magnitude peak value in the time domain;
     c) compute $\hat{\sigma}(f, \theta, p)$ using (2);
   end
   end

Output target RCS as a function of frequency over different aspect angles.

measured data is related to the SNR (expressed in linear unit) via

$$\Delta\sigma = -20 \operatorname{Log}\left(1 - \frac{1}{\text{SNR}}\right). \tag{3}$$

For the case at hand, the noise-induced measurement uncertainty, computed according to (3), is reasonably in the range $0.03 - 0.72$ dB for the interval $8.2 - 12.4$ GHz, and $0.01 - 0.11$ dB for the $12.4 - 18$ GHz bandwidth. Therefore, the data reported in Fig. 3 comply with the resulting confidence intervals, and the occurrence of a few outliers is likely to be related to the worst-case event where the largest error is experienced in both the reference and test measurements.

It is also worth mentioning that, while the SNR plays a key role in the measurement uncertainties experienced in the current setup, additional experimental setup limitations due to difference in the average illumination (between measurements of the drones and the calibration target) [29], background-target interaction, imbalance between in-phase and quadrature components, and near field acquisition, just to mention a few, are always present [29], although difficult to quantify accurately.

III. DRONE RCS STATISTICAL BEHAVIOR

The classic approach for evaluating radar detection performance is based on the assumption that the target's RCS fluctuation follows one of the Swerling models I-V [27]. However, as confirmed by some practical cases, amplitude fluctuations do not always comply with the aforementioned models, resulting in a mismatch between the actual and the theoretical radar performance. Indeed, several alternative fluctuation models (e.g., Weibull, Log-normal, shadowed Rice, two-state Rayleigh-chi, just to mention a few) have been proposed in the open literature to cope with this problem [27],

[34], [35]. Using a suitable statistical description for the target RCS behavior enables the accurate prediction of radar detection performance as well as the design of appropriate signal processing architectures. Toward this goal, in this section, the measured RCS signatures of several drones are statistically analyzed by fitting the data with well-known and commonly used distributions (at most bi-parametric), over different frequencies and polarizations. Then, the most appropriate statistical model for each drone RCS collection (in the aspect angle domain) is selected resorting to the CVM distance and the KS test.

The RCS analysis of the AscTec Firefly is discussed in Subsection III-A, then the other drones are studied in Subsection III-B.

A. Statistical Analysis of AscTec Firefly RCS

A detailed analysis of the AscTec Firefly's RCS is provided in this subsection. Before proceeding further, it is worth mentioning that the worst case noise power (averaged over the two polarizations) observed in the measurements, after pre-processing, subband analysis, and calibration, is $N_F \approx -34.5$ dBsm for the frequency band $8.2 - 12.4$ GHz, and $N_F \approx -44.5$ dBsm for the interval $12.4 - 18$ GHz. Given the noise level N_F, an estimate of the measurements SNR in a given frequency bin, which provides insights on the measurement accuracy (see (3)), is given by the ratio between the target RCS and N_F, i.e., it can be practically computed as $SNR(f,p) = \hat{\sigma}(f,p)/N_F$. For the case at hand, apart for a few outliers, the SNR is in the order of 20 dB, corresponding to a $\Delta\sigma < 0.09$ dB.

As to the RCS, Fig. 4 displays both the mean and standard deviation values (with respect to aspect angle) versus frequency, with reference to both HH and VV RCS acquisitions. Remarkably, similar average RCS values are obtained in both the HH and VV polarizations, in agreement with [7]. The plots also reveal that, for a given frequency bin, the standard deviation of the measured RCS is about 15 dBsm, which might be attributed to the presence of a few major scatterers whose interaction significantly changes with aspect angles. This behavior is supported by Fig. 5, which illustrates the RCS of the drone in polar coordinates (at varying azimuthal angles) for HH polarization and different central frequencies, i.e., 9.5 GHz, 10.7 GHz, 14.1 GHz, and 15.9 GHz. Actually, the figure highlights that the RCS is characterized by a fast fluctuation in angle. As already said, this behavior is mainly determined by the composition of the dominant scatterers returns.

Let us now focus on the first-order statistical analysis. Since the drone RCS strongly changes with aspect angle, it appears reasonable the exploitation of a statistical model to describe the target fluctuation and accurately predict radar detection performance. Indeed, even if the actual RCS of the drone is a deterministic quantity[4], due to the unknown target aspect angle, it can be treated as a random variable so as to capture its ensemble behaviour.

---

[4]It is worth noting that the RCS of a flying drone is likely to exhibit a dynamic behavior due to vibrations, internal structural bending, and changes in orientation induced by possible turbulent atmosphere.
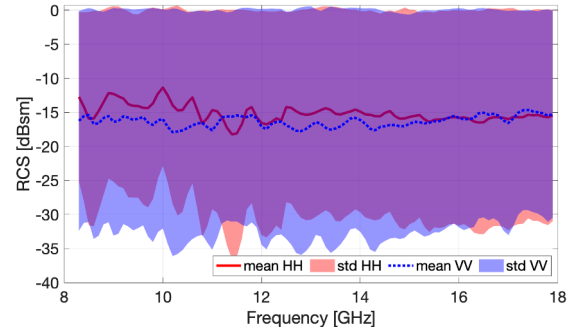

Fig. 4. Mean values of AscTec Firefly's RCS versus frequency for HH and VV polarizations (solid and dashed lines, respectively). The top (bottom) border of the shaded area represents the mean value plus (minus) standard deviation.
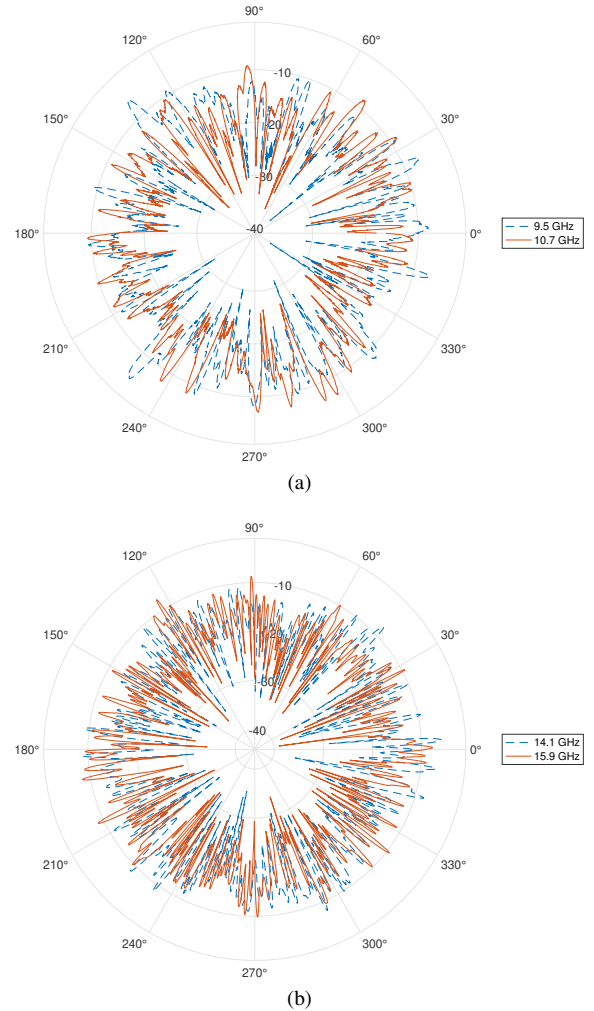

(a)

(b)

Fig. 5. Polar plot of AscTec Firefly RCS [dBsm] for HH polarization in the frequency bin with central frequency: (a) 9.5 GHz (blue curve) and 10.7 GHz (red curve), (b) 14.1 GHz (blue curve) and 15.9 GHz (red curve).

Inspired by previous studies on target RCS fluctuation statistics, in this paper the distributions (at most bi-parametric[5]) reported in Table III are studied to model the RCS of the AscTec Firefly. In the table, $\Gamma(x)$, $\gamma(a,b)$, and $\mathrm{erf}(x)$ indicate the Gamma, the incomplete Gamma, and the error functions, respectively.

The fitting of the above-mentioned distributions with the data is performed considering the RCS measurements for different aspect angles at a given frequency f and in a polarization $p = \{HH, VV\}$. Formally, the parameter vector of the distributions is determined as a solution to the following optimization problem

$$\widehat{\boldsymbol{\theta}}(f,p) = \arg\min_{\boldsymbol{\theta}} CVM(\hat{\boldsymbol{\sigma}}(f,p), F(x;\boldsymbol{\theta})) \qquad (4)$$

where $F(x;\boldsymbol{\theta})$ is the CDF of the distribution under test, $\boldsymbol{\theta}$ denotes the distributional parameters, $\hat{\boldsymbol{\sigma}}(f,p) = [\hat{\sigma}_1(f,p), \hat{\sigma}_2(f,p), \ldots, \hat{\sigma}_n(f,p)]^{\mathrm{T}} \in \mathbb{R}^n$, with $n = 3600$, is the vector of the measured/observed RCS, and [36]

$$CVM(\hat{\boldsymbol{\sigma}}(f,p), F(x;\boldsymbol{\theta})) =$$
$$\sqrt{\frac{1}{12n} + \sum_{i=1}^{n}\left[\frac{2i-1}{2n} - F(\hat{\sigma}_i(f,p);\boldsymbol{\theta})\right]^2} \qquad (5)$$

is the CVM distance, with $(\cdot)^{\mathrm{T}}$ being the transpose operator and $\mathbb{R}^N$ the set of N-dimensional column vectors of real numbers. The optimization problem in (4) is tackled by means of the iterative algorithm proposed in [37] which is implemented in MATLAB with the function *fminsearch*, using as initial estimates of the distributional parameters those obtained via the MATLAB function *fitdist*. Fig. 6 displays the CVM distances between the optimally fitted (according to (4)) distributions and the empirical CDF for different frequencies, whereas the average CVM distances are reported in Table IV. Inspection of the table reveals that the Gamma CDF in general achieves the lowest average CVM distance from the measured data, whereas the Weibull distribution ranks second. Hence, to confirm the quality of the aforementioned model to faithfully describe the collected data, a KS test is performed [36], [38]. This is a non parametric statistical procedure which can be used to assess the goodness-of-fit between the empirical and the theoretical RCS distributions, i.e., it tests the simple hypothesis[6]

$$\mathcal{H}_0 : \hat{\sigma}_i(f,p) \text{ has the CDF } F(x;\widehat{\boldsymbol{\theta}}(f,p)), \ p = \{HH, VV\}. \tag{6}$$

Since the KS test requires independent observations, before evaluating the KS statistics the RCS data have been decimated to ensure a certain degree of data uncorrelation, and hopefully independence among the measurements. Specifically, a decimation factor of 36 (corresponding to a step of 3.6 degree) has been considered, resulting for each drone RCS dataset in an average (over the frequencies) one-lag correlation coefficient

[5]Distribution models with more than two parameters might result in overfitting issues, which are not addressed in the present study.

[6]Notice that when KS is used with estimated parameters from the data as in (6), the test cannot theoretically be used in its basic form [39].

close to 0.5. This value is compatible with that provided by the approximated expression [27]

$$\Delta\theta = \frac{c}{2Lf} \tag{7}$$

where c is the speed of light and L is a characteristic linear length of the UAV.

In a nutshell, the KS test tackles the hypothesis testing problem (6) by comparing a threshold with the largest absolute difference between the empirical CDF of the data and the theoretical one. Formally,

$$D_n(f,p) \underset{\mathcal{H}_0}{\overset{\mathcal{H}_1}{\gtrless}} \gamma(\alpha_{KS}) \tag{8}$$

where

$$D_n(f,p) = \sup_{\hat{\sigma}_i(f,p) \in \hat{\boldsymbol{\sigma}}(f,p)} \left| \hat{F}(\hat{\sigma}_i(f,p)) - F(\hat{\sigma}_i(f,p);\boldsymbol{\theta}) \right| \tag{9}$$

with $\hat{F}(\hat{\sigma}_i(f,p))$ the empirical CDF at a given frequency and polarization of the measured RCS values (for different aspect angles) collected in the vector $\hat{\boldsymbol{\sigma}}(f,p)$, whereas $\gamma(\alpha_{KS})$ is the decision threshold (which does not depend on the tested distribution) set to ensure the desired significance level α_{KS}. Besides, the implementation of (8) is tantamount to comparing the p-value of $D_n(f,p)$, under the null hypothesis, with α_{KS} [40]. Fig. 7 illustrates the outcomes of the KS tests in terms of p-values along with the desired significance level $\alpha_{KS} = 0.01$. Looking over the plots unveils that, regardless of the frequency and the polarization, the resulting p-values are always greater than the significance level. As a consequence, the $\mathcal{H}_0$ hypothesis cannot be rejected.

To gather further insights in the fitting procedure, the Quantile-Quantile (QQ) plot [41], [42], displaying the quantiles of the empirical distribution against those of the fitted Gamma model, are reported in Fig. 8 with reference to the data corresponding to the maximum and minimum p-value, which, for the case study at hand, are achieved at VV polarization in bins with center frequencies 14.4 GHz and 10.10 GHz, respectively. Precisely, the red curve is the line connecting the points $(Q_G 25\%, Q_E 25\%)$ and $(Q_G 75\%, Q_E 75\%)$, with $Q_G X\%$ and $Q_E X\%$ the Xth percentiles of the fitted Gamma and the empirical distributions, respectively, whilst the blue curve is the QQ plot. The curves are close to the bisector, indicating that the fitted models adequately describe the measured data in the examined cases.

Finally, Fig. 9 concludes this subsection with the analysis of the Gamma parameters obtained with the fitting procedure. In particular, Fig. 9(a) compares the sample mean of the measured RCS with the first moment of the fitted Gamma distribution. The results show that Gamma expectation is very close to the mean RCS $\tilde{\sigma}_p$, $p = \{HH, VV\}$ of the drone. The shape parameter of the optimally fitted Gamma is examined in Fig. 9(b) versus the frequency. A close examination of the figure reveals that the shape parameter is relatively close to 1, indicating that the RCSs can be well represented using a statistical distribution close to an Exponential (Swerling I-II) model. However, based on the results shown in Fig. 6 and Table IV, a plain Exponential distribution is unable to

TABLE III
CDFs OF THE CONSIDERED MODELS.

Distribution	CDF	Parameter 1	Parameter 2	Mean
Exponential	$F(x; \lambda) = 1 - e^{-\lambda x}, x \geq 0$	$\lambda > 0$, rate	-	$\mu = 1/\lambda$
Gamma	$F(x; \alpha, \beta) = \frac{1}{\Gamma(\alpha)} \gamma\left(\alpha, \frac{x}{\beta}\right), x \geq 0$	$\alpha > 0$, shape	$\beta > 0$, scale	$\mu = \alpha\beta$
LogNormal	$F(x; \chi, \sigma) = \frac{1}{2}\left[1 + \mathrm{erf}\left(\frac{\ln x - \chi}{\sigma\sqrt{2}}\right)\right], x > 0$	$\chi \in (-\infty, +\infty)$	$\sigma > 0$	$\mu = e^{\chi + \frac{\sigma^2}{2}}$
Weibull	$F(x; a, b) = 1 - e^{-(x/a)^b}, x \geq 0$	$a \in (0, +\infty)$, scale	$b \in (0, +\infty)$, shape	$\mu = a\Gamma(1 + 1/b)$

fully predict the behavior of the measured data, and a bi-parametric distribution, i.e., the Gamma, appears necessary to better capture the data statistical properties.

TABLE IV
MEAN CVM DISTANCES BETWEEN EMPIRICAL AND THEORETICAL CDF OF ASCTEC FIREFLY'S RCS.

Distribution	mean CVM HH	mean CVM VV
Exponential	0.93	0.73
Gamma	0.59	0.49
LogNormal	1.11	1.37
Weibull	0.63	0.50

B. Statistical Analysis of Others Drones RCS

In this subsection, the statistical analysis is conducted on the collected RCSs of the other tested drones[7] (see Table II). Fig. 10 shows the mean and standard deviation values of the RCS versus frequency for HH and VV polarizations. Like the results obtained for the AscTec Firefly (see Fig. 4), the considered drones achieve similar RCS values in both HH and VV polarizations. Moreover, large fluctuations in the RCS values can be observed, with a standard deviation in the order of 10 dBsm for the AscTec Pelican and DJI Matrice 100 (Figs. 10(a) and 10(d)) and 20 dBsm for the Venom VN10 and the Parrot AR.DRONE 2.0 (Figs. 10(b) and 10(c)). As to the statistical analysis, Table V reports the mean values (over the frequency) of the CVM distances computed between the empirical and theoretical CDFs of the measured RCSs in both HH and VV polarizations. Interestingly, the Gamma model is still able to achieve the lowest average CVM distance in almost all the scenarios, with some exceptions where Weibull distribution prevails over the others (see for instance the case of Asctec Pelican in HH or Venom VN10 in VV). However, under these specific instances, the mean CVM distances achieved by the Gamma and the Weibull model are relatively close. Moreover, unlike the Weibull, the Gamma fluctuation law enables a quite simple and closed-form analytical evaluation of the detection performance [35].

Fig. 11 shows the shape parameter values of the fitted Gamma versus frequency for both polarizations. For almost all the cases, the Gamma shape parameter is close to 1, underlining that the measured RCS first-order statistics are not far from an Exponential-like behavior. The only exception

which is worth a further investigation is the AscTec Pelican. As a matter of fact, Fig. 11(a) reveals that for the frequency bands $10.2 - 10.8$ GHz and VV polarization, the Gamma shape parameter is close to 2, meaning that the fluctuation follows a chi-squared distribution with 4 degrees of freedom. Remarkably, this latter distribution (used in the Swerling 3 and 4 models) is typically employed to model targets composed of scatterers of similar strength plus one dominant scatterer, with the latter having RCS $1 + \sqrt{2}\sigma_o$, where σ_o is the sum of RCS of the randomly distributed equal-strength scatterers [27].

IV. RADAR DETECTION PERFORMANCE

In this section, the radar capabilities to detect UAVs is analyzed by comparing performance under experimental target fluctuations with that resulting from appropriate statistical models. In particular, due to the huge fluctuations in RCS and hence in the resulting SNR of the received radar signal, the detection performance would also be extremely dependent on the aspect angle. This poses a severe problem in the evaluation of the radar performance because the exact computation for each angle is both complicated and of no practical utility (a perfect knowledge/estimate of the target aspect angle must be available) [27]. Therefore, an average performance based on a statistical model for the target RCS (modeled as a random variable) is a viable mean to carry out a detection analysis [43]–[45]. In this respect, it is assumed that the target's scatterers, whose composition determines the RCS value, are all within a resolution cell. The Probability of Detection (P_D), computed assuming a desired Probability of False Alarm $P_{fa} = 10^{-4}$, is used as performance metric.

In the following, it assumed that a standard pulse-Doppler radar illuminates the target (in the Fraunhofer region) for a CPI $\tilde{T} = MT$, with M the number of pulses and T the Pulse Repetition Interval (PRI). It is assumed that the azimuth aspect angle of the drone is constant within the CPI, namely, the target amplitude does not change from pulse to pulse. Therefore, for a radar operating with a carrier frequency f and polarization $p = \{HH, VV\}$, the received signal can be modeled as

$$\boldsymbol{r} = a(\theta, f, p)e^{j\phi}\boldsymbol{s} + \boldsymbol{n} \tag{10}$$

where

- $a(\theta, f, p)$ denotes the useful signal strength which accounts for the target RCS (at aspect angle θ) and the other terms involved in the radar equation;
- ϕ accounts for the target phase response, including the target range, and it is assumed uniformly distributed over $[0, 2\pi]$;

---

[7]For the case of DJI Matrice 100, to ensure that it may be approximated as a point-like reflector, frequency bins 100 MHz wide have been used, corresponding to a range resolution of 1.5 m.
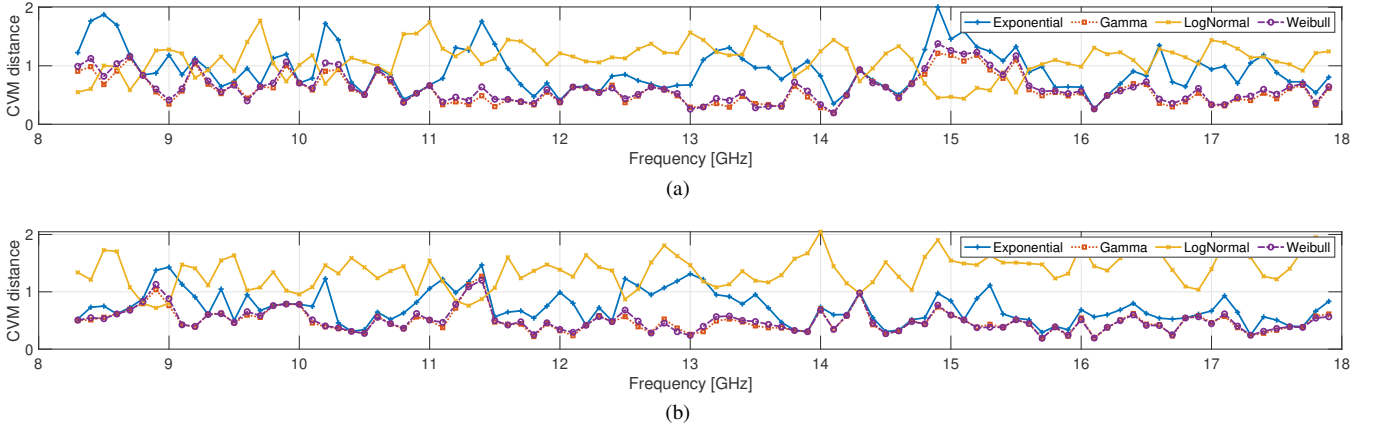
Fig. 6. CVM distances between the empirical and the theoretical CDFs for the measured RCS of AscTec Firefly: (a) HH polarization, (b) VV polarization.

TABLE V
MEAN CVM DISTANCES BETWEEN EMPIRICAL AND THEORETICAL CDF.

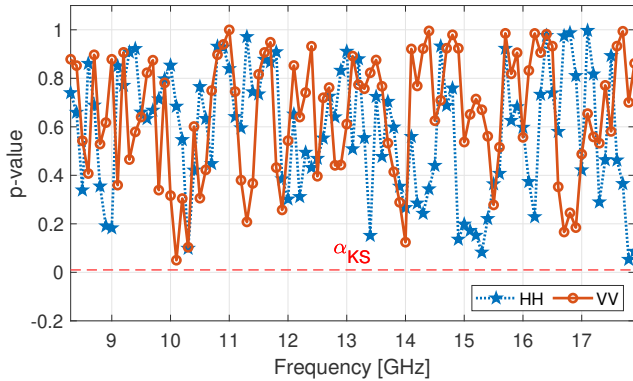| Distribution | mean CVM distance HH / VV | | | | |
	AscTec Firefly	AscTec Pelican	Venom VN10	Parrot AR.DRONE 2.0	DJI Matrice 100
Exponential	0.93 / 0.73	1.21 / 1.43	1.17 / 1.08	0.93 / 0.99	0.85 / 0.77
Gamma	**0.59 / 0.49**	0.73 / **0.66**	**0.62** / 0.69	**0.66 / 0.57**	**0.62 / 0.55**
LogNormal	1.11 / 1.37	1.09 / 1.15	1.26 / 1.32	1.06 / 1.21	0.98 / 1.04
Weibull	0.63 / 0.50	**0.67** / 0.68	0.65 / **0.66**	0.67 / 0.58	0.64 / 0.58

Fig. 7. P-values resulting from the KS test for Gamma distribution versus the AscTec Firefly's RCS measurements. The significance level (dashed red curve) $\alpha_{KS} = 0.01$, is reported as a reference.

- $s = [1, e^{j2\pi f_d T}, \ldots, e^{j2\pi f_d (M-1)T}]^{\mathrm{T}}$ represents the Doppler steering vector evaluated in correspondence of the Doppler frequency f_d (assumed known), with $j = \sqrt{-1}$;
- $n \sim CN(0, \sigma_n^2 I)$ is the interference plus noise contribution, modeled as a zero-mean complex circularly symmetric Gaussian random vector, with covariance matrix $\sigma_n^2 I$; therein, σ_n^2 is the noise power level assumed, without loss of generality, equal to 0 dB.

For the case at hand, the optimum coherent detector is given by [27]

$$|s^\dagger r| \underset{\mathcal{H}_0}{\overset{\mathcal{H}_1}{\gtrless}} \zeta \qquad (11)$$

where $(\cdot)^\dagger$ denotes the conjugate transpose operator, $\mathcal{H}_0$ and $\mathcal{H}_1$ indicate the null and the alternative hypothesis (i.e., target

echo absence/presence within the received observation vector), respectively, and ζ is the detection threshold set to ensure the desired P_{fa}.

Let us define the actual integrated SNR for the specific target aspect angle θ, as

$$\mathrm{SNR}_c(\theta, f, p) = \overline{\mathrm{SNR}}_c \frac{\sigma(\theta, f, p)}{\tilde{\sigma}(f, p)} \qquad (12)$$

with $\overline{\mathrm{SNR}}_c$ the average integrated SNR over all aspect angles and $\tilde{\sigma}(f, p)$ the mean target RCS value. Then, the probability of detection for the decision rule in (11) at the aspect angle θ can be obtained as [27]

$$\mathrm{P_D}(\overline{\mathrm{SNR}}_c, \theta, f, p) = Q\left(\sqrt{2\overline{\mathrm{SNR}}_c \frac{\sigma(\theta, f, p)}{\tilde{\sigma}(f, p)}}, \sqrt{-2\log P_{fa}}\right) \qquad (13)$$

with $Q(\cdot)$ denoting the Marcum Q function [46]. Hence, the mean detection performance over the aspect angle at given carrier frequency f and polarization p can be computed averaging (13) over all the looking angles, i.e.,

$$\mathrm{P_D}(\overline{\mathrm{SNR}}_c, f, p) = \frac{1}{3600} \sum_{\theta \in \mathbb{T}} \mathrm{P_D}(\overline{\mathrm{SNR}}_c, \theta, f, p) \qquad (14)$$

where $\mathbb{T} = \{i \times 0.1, i = 0, \ldots, 3599\}$.

To validate the fluctuation models inferred in Section III, the resulting average $\mathrm{P_D}$ for each theoretical distribution are considered. Specifically, the $\mathrm{P_D}$ corresponding to the Gamma fluctuation model (whose closed-form expression is available in [35]) is estimated via standard Monte Carlo counting techniques over 10^4 independent trials, with the integrated SNR given by

$$\mathrm{SNR}_c(\theta, f, p) = \overline{\mathrm{SNR}}_c \frac{\rho(f, p)}{\mu(f, p)} \qquad (15)$$
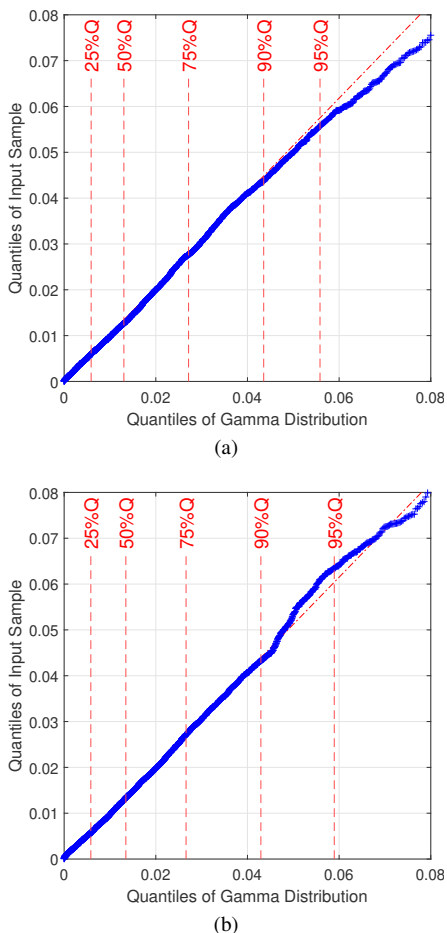
Fig. 8. QQ plots of measured RCS of AscTec Firefly versus Gamma distribution with fitted parameters for two frequency bins in VV polarization: (a) 14.4 GHz, (b) 10.10 GHz. The corresponding p-values are: (a) 0.995, (b) 0.050.
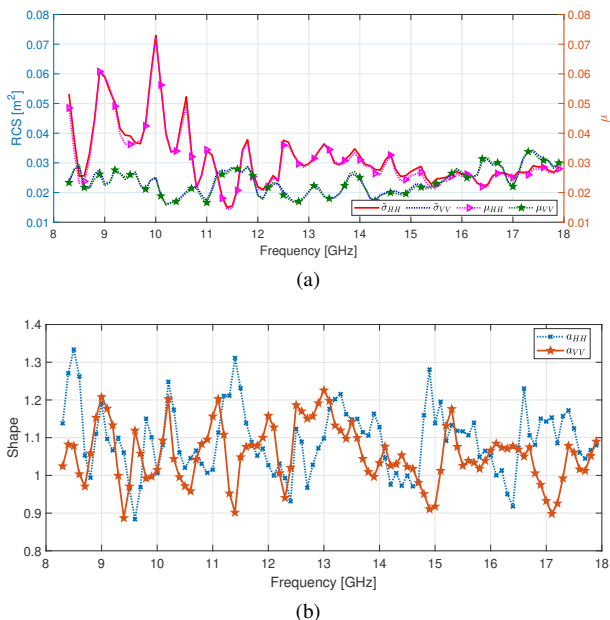

Fig. 9. Analysis of the Gamma distribution's parameters versus frequency, fitted with the RCS measurements of AscTec Firefly. (a) Comparison between the mean RCS values and the expectation of the fitted Gamma distribution versus frequency for HH and VV polarization; (b) Gamma shape parameter values versus frequency.

where $\rho(f,p)$ is randomly drawn from a Gamma distribution with parameters $\boldsymbol{\theta}(f,p) = [\alpha(f,p), \beta(f,p)]$, inferred from the fitting procedure, whereas $\mu(f,p)$ denotes its corresponding expected value, i.e., $\mu(f,p) = \alpha(f,p)\,\beta(f,p)$. Therefore, it results in an average $\mathrm{P_D}$

$$\mathrm{P_D}(\overline{\mathrm{SNR}}_c, f, p) = \frac{1}{10^4} \sum_{i=1}^{10^4} Q\left(\sqrt{2\overline{\mathrm{SNR}}_c \frac{\rho(f,p)}{\mu(f,p)}}, \sqrt{-2\log P_{fa}} \right). \tag{16}$$

For comparison purposes, the $\mathrm{P_D}$ curves $\mathrm{P_{D\,SW0}}$ and $\mathrm{P_{D\,SW1}}$ for non-fluctuating (SW0) and fluctuating (SW1) targets, respectively, are also included, where [27]

$$\mathrm{P_{D\,SW0}}(\overline{\mathrm{SNR}}_c) = Q\left(\sqrt{2\overline{\mathrm{SNR}}_c}, \sqrt{-2\log P_{fa}} \right) \tag{17}$$

and

$$\mathrm{P_{D\,SW1}}(\overline{\mathrm{SNR}}_c) = P_{fa}^{1/(1+\overline{\mathrm{SNR}}_c)}. \tag{18}$$

$\mathrm{P_D}$ versus $\overline{\mathrm{SNR}}_c$ related to the AscTec Firefly is displayed in Fig. 12 for four different frequencies, i.e., 12(a) 14.1 GHz, 12(b) 15.9 GHz, 12(c) 8.5 GHz, and 12(d) 17.1 GHz. The values of the involved Gamma shape parameter are reported in Table VI. Specifically, Figs. 12(a) and 12(b) consider the scenario of Exponential-like RCS fluctuation behavior, i.e., $\alpha \approx 1$, whilst Fig. 12(c) and Fig. 12(d) refer respectively to the largest and the lowest values of the shape parameter, which are achieved, for this UAV, at the polarization HH and VV, respectively (see Table VI). The figure shows nearly perfect adherence (with negligible displacements) between the $\mathrm{P_D}$ curves obtained using measured and simulated data in all the reported cases, proving that, also from a radar detection standpoint, the fitted Gamma distribution is able to describe the measured data. Furthermore, the results outline that the $\mathrm{P_D}$ curves pertaining to the drone data are always distant from the SW0 benchmark, but quite close to those of the SW1 model. This emerging trend is expected given the observed RCS Exponential-like fluctuation characteristics highlighted in Section III. In this regard, the results clearly pinpoint that when α is close to 1 (see Figs. 12(a) and 12(b)), the standard SW1 model provides accurate performance prediction. Conversely, the more the shape parameter value deviates from 1, the larger the discrepancy between the predicted performance with the SW1 model and the actual one. Unarguably, the 1.5 dB $\overline{\mathrm{SNR}}_c$ difference at $\mathrm{P_D} = 0.9$ between the aforementioned curves (in HH), illustrated in Figs. 12(c) and 12(d), standouts that there are specific circumstances where the performance predicted with the SW1 model leads to an inaccurate performance estimate of the radar detection task. The larger the value of α (provided that $\alpha > 1$), the larger the underestimate. In similar manner, as α approaches 0, the overestimation increases.

To further analyze the cases reported in Table VI, the radar detection performance is studied versus the aspect angle, assuming $\overline{\mathrm{SNR}}_c = 13$ dB, in Figs. 13 and 14, which refer to the HH and VV polarization, respectively. Moreover, both the SW1 benchmark and the average $\mathrm{P_D}$ value (14) are reported for comparison purposes. As expected, regardless of the frequency and the polarization, the $\mathrm{P_D}$ fluctuates as the aspect angle varies, but reaches, in most cases, performance saturation with $\mathrm{P_D} = 1$. Conversely, cases where worse performance are
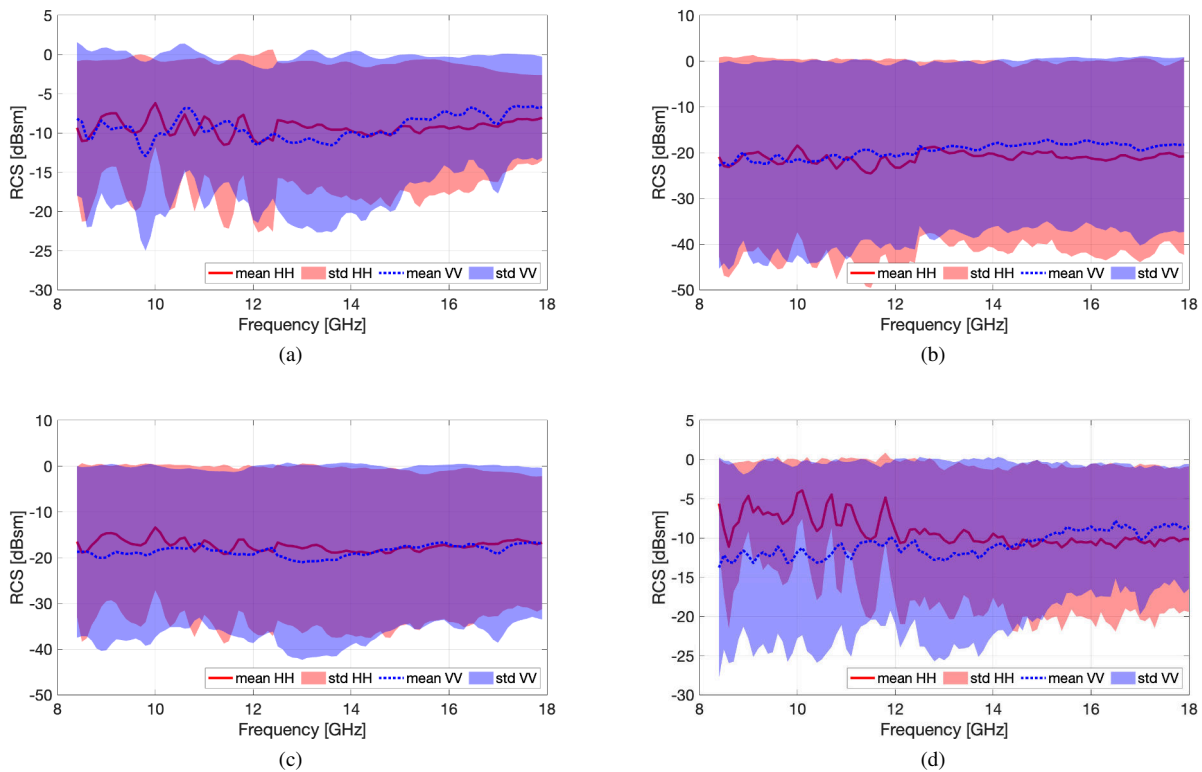
Fig. 10. RCS mean and standard deviation values versus frequency for a) AscTec Pelican, b) Venom VN10, c) Parrot AR.DRONE 2.0, d) DJI Matrice 100.
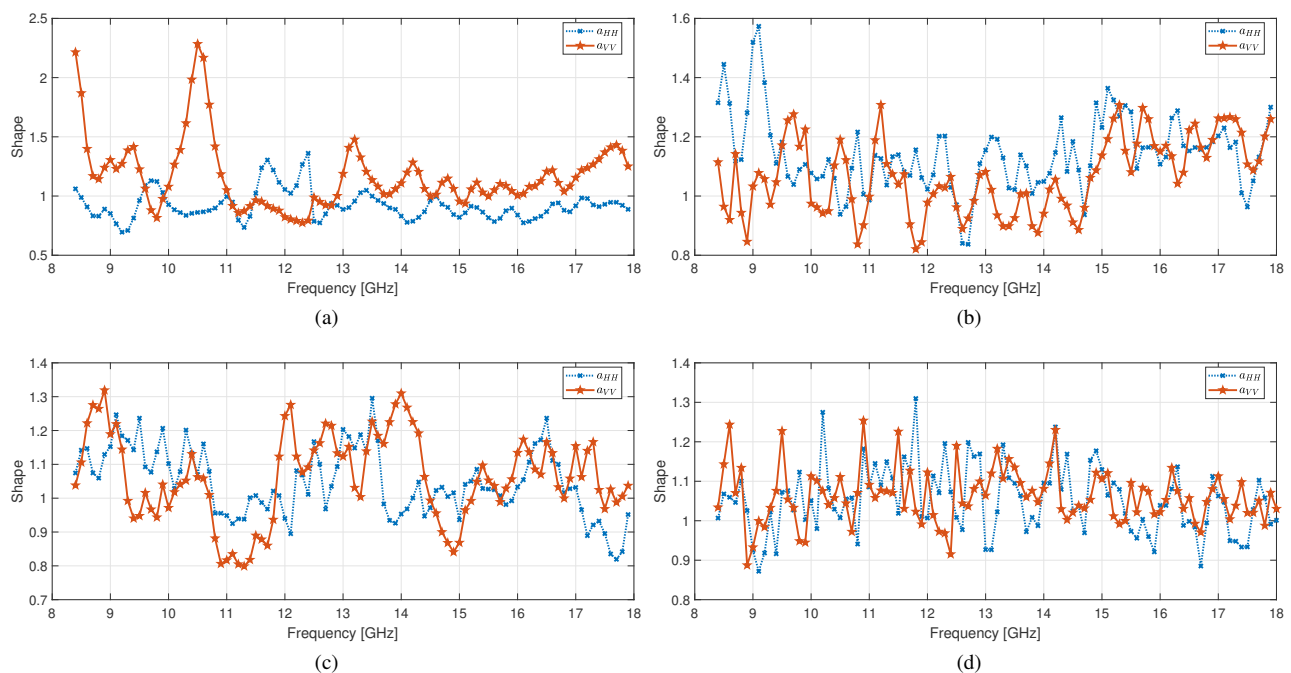

Fig. 11. Shape parameter values of the Gamma distribution fitted with the RCS data of a) AscTec Pelican, b) Venom VN10, c) Parrot AR.DRONE 2.0, d) DJI Matrice 100, versus frequency in HH and VV polarization.

experienced, with values below 0.1, are restricted to a few particular aspect angles. However, according to the previous analysis, the achieved average P_D is close to 0.65.

In Table VII, the average P_D values obtained for $\overline{SNR}_c = \{5, 13\}$ dB leveraging the other collected drones RCS data, with reference to the two polarizations and different frequencies, i.e., $\{9, 11, 13, 15, 17\}$ GHz, are compared with those obtained with the SW1 model. The actual performance is very close to the theoretical counterpart in almost all the reported cases, with differences from SW1 in the order of 0.01 for $\overline{SNR}_c = 5$ dB and less than 0.05 (except for some outliers) for $\overline{SNR}_c = 13$ dB. Thus, the trends of Figs. 12(a) and 12(b) are confirmed by these new achievements, i.e., the SW1 model yields an accurate performance prediction, as long as the shape parameter is close to 1. Again, particular attention should be paid to the cases where the shape parameter α of the fitted Gamma model deviates from 1. Some instances falling into this last scenario are analyzed in Fig. 15; therein (see Table VIII for the corresponding values of the Gamma shape parameter) Fig. 15(a) refers to the Venom VN10 at 9.1 GHz, Fig. 15(b) shows the Parrot AR.DRONE at 14 GHz, Figs. 15(c) and 15(d) consider the AscTec Pelican at 9.2 GHz and 10.5 GHz, respectively. In all the examined cases, a discrepancy between the actual and the SW1 performance curves is clearly experienced in both polarizations. This behavior, previously analyzed in Figs. 12(c) and 12(d), is again reflected in the results under investigation pertaining to the other drones, which further corroborates the requirement for tailored (bi-parametric) fluctuation models to accurately predict the UAVs radar detection performance.

TABLE VI
VALUES OF THE GAMMA SHAPE PARAMETER FOR THE FREQUENCIES
ANALYZED IN FIG. 12.

Frequency	α_{HH}	α_{VV}
14.1 GHz	1.05	1.08
15.9 GHz	1.07	1.04
8.5 GHz	1.33	1.08
17.1 GHz	1.15	0.9

V. CONCLUSION

This paper has considered the radar detection performance prediction leveraging measured RCS of small UAVs collected in a semi-controlled environment as a function of frequency, angle, and polarization. Specifically, RCS measurements from five drones of different sizes and characteristics have been acquired in the frequency range 8.2-18 GHz. Hence a statistical analysis over a moving bandwidth of 200 MHz has been performed checking the adequacy of some distributions (at most bi-parametric) to describe the first-order RCS statistics. The results have highlighted that, in the considered frequency bands, the RCSs of the drones assume quite small values and are characterized by strong fluctuations in angle. Besides, from a statistical standpoint, the Gamma distribution proved capable of modeling such measurement variability, characterized, in the majority of cases, by Exponential-like fluctuations. Precisely, the RCS variability can be usually described using Gamma shape parameter values close to 1. The detection performance has been evaluated using both collected and simulated data (via Monte Carlo counting technique) considering as terms of comparison the standard Swerling 0 and Swerling 1 models. Usually, the curves exhibit performance deviations in the order of dB fractions from the Rayleigh fluctuating target case.

Future research avenues might consider further statistical analyses including RCS measurements collected in cross-polarization as well as the investigation of the corresponding radar detection performance by resorting to a full polarimetric processing architecture. Finally, it is of particular interest the extension of the measurement campaign to include data collection at elevation angles within the interval 0-10 degrees, which are relevant for typical anti-drone search radar applications.

REFERENCES

[1] M. Rosamilia, A. Aubry, A. Balleri, V. Carotenuto, and A. De Maio, "RCS measurements of UAVs and their statistical analysis," in *2022 IEEE 9th International Workshop on Metrology for AeroSpace (MetroAeroSpace)*, 2022, pp. 179–184.

[2] M. Rosamilia, A. Aubry, A. Balleri, V. Carotenuto, and A. De Maio, "Performance prediction of the coherent radar detector on measured UAVs data," in *Radar 2022 International Conference on Radar Systems*, 2022.

[3] J. Gong, J. Yan, D. Li, D. Kong, and H. Hu, "Interference of radar detection of drones by birds," *Progress In Electromagnetics Research M*, vol. 81, pp. 1–11, 2019.

[4] S. Rahman and D. A. Robertson, "In-flight RCS measurements of drones and birds at K-band and W-band," *IET Radar, Sonar & Navigation*, vol. 13, no. 2, pp. 300–309, Feb. 2019.

[5] J. Wang, Y. Liu, and H. Song, "Counter-unmanned aircraft system(s) (C-UAS): State of the art, challenges, and future trends," *IEEE Aerospace and Electronic Systems Magazine*, vol. 36, no. 3, pp. 4–29, 2021.

[6] I. Guvenc, F. Koohifar, S. Singh, M. L. Sichitiu, and D. Matolak, "Detection, tracking, and interdiction for amateur drones," *IEEE Communications Magazine*, vol. 56, no. 4, pp. 75–81, 2018.

[7] M. Pieraccini, L. Miccinesi, and N. Rojhani, "RCS measurements and ISAR images of small UAVs," *IEEE Aerosp. Electron. Syst. Magazine*, vol. 32, no. 9, pp. 28–32, 2017.

[8] C. J. Li and H. Ling, "An investigation on the radar signatures of small consumer drones," *IEEE Antennas and Wireless Propagation Letters*, vol. 16, pp. 649–652, 2017.

[9] M. Ezuma, C. K. Anjinappa, M. Funderburk, and I. Guvenc, "Radar cross section based statistical recognition of UAVs at microwave frequencies," *IEEE Trans. Aerosp. Electron. Syst.*, vol. 58, no. 1, pp. 27–46, 2022.

[10] A. Herschfelt, C. R. Birtcher, R. M. Gutierrez, Y. Rong, H. Yu, C. A. Balanis, and D. W. Bliss, "Consumer-grade drone radar cross-section and micro-doppler phenomenology," in *2017 IEEE Radar Conference (RadarConf)*, 2017, pp. 0981–0985.

[11] V. Semkin, J. Haarla, T. Pairon, C. Slezak, S. Rangan, V. Viikari, and C. Oestges, "Analyzing radar cross section signatures of diverse drone models at mmWave frequencies," *IEEE Access*, vol. 8, pp. 48958–48969, 2020.

[12] L. To, A. Bati, and D. Hilliard, "Radar cross section measurements of small unmanned air vehicle systems in non-cooperative field environments," in *2009 3rd European Conference on Antennas and Propagation*, 2009, pp. 3637–3641.

[13] J. Ochodnický, Z. Matousek, M. Babjak, and J. Kurty, "Drone detection by Ku-band battlefield radar," in *2017 International Conference on Military Technologies (ICMT)*, 2017, pp. 613–616.
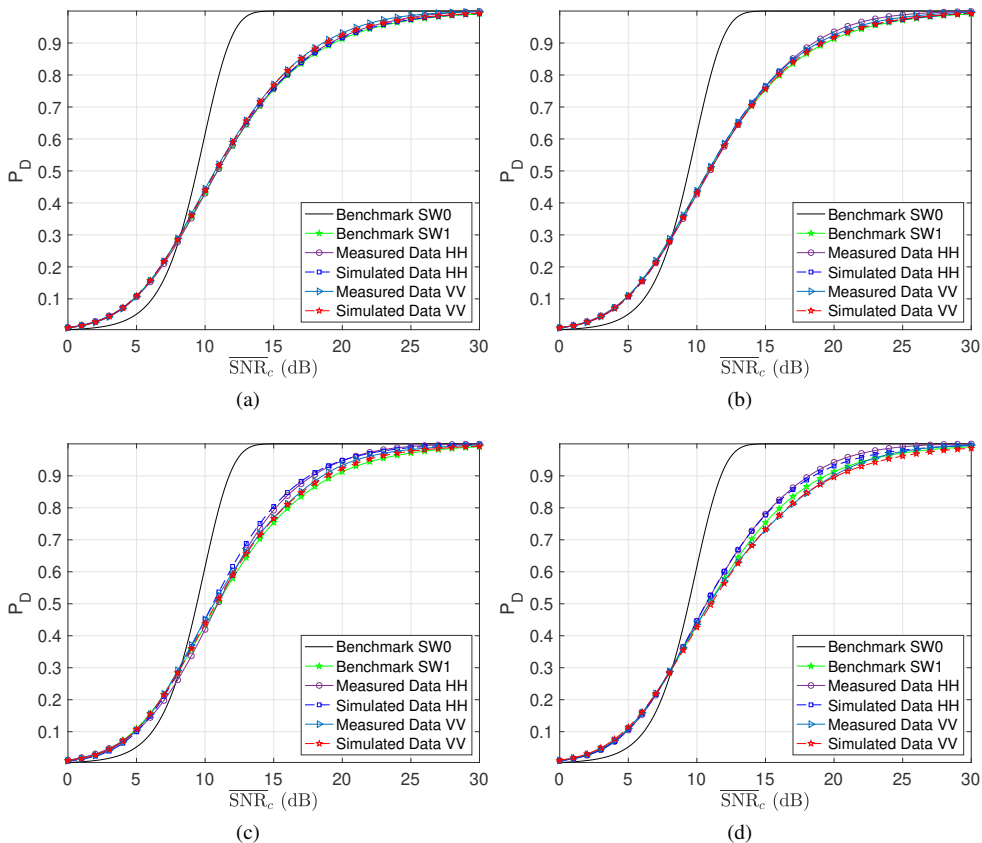
Fig. 12. P_D versus $\overline{\text{SNR}}_c$ curves using measured and simulated AscTec Firefly data for HH and VV polarization in the frequency bin with central frequency: (a) 14.1 GHz, (b) 15.9 GHz, (c) 8.5 GHz, and (d) 17.1 GHz.
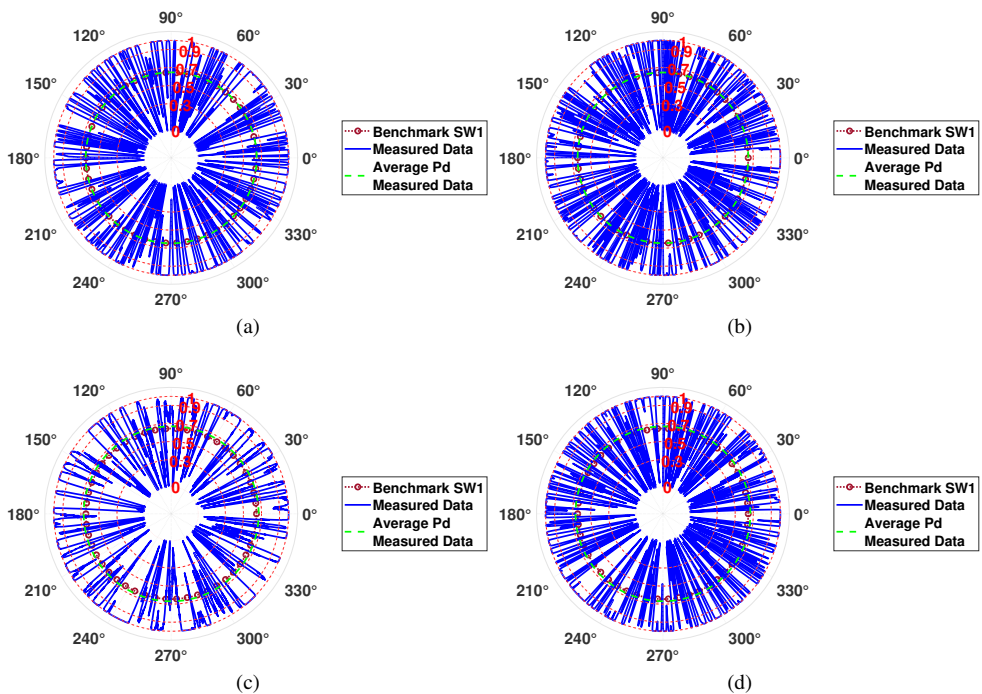

Fig. 13. P_D over aspect angles curves using measured and simulated AscTec Firefly data for $\overline{\text{SNR}}_c = 13$ dB in HH polarization. The plots refer to the frequency bin with central frequency: (a) 14.1 GHz, (b) 15.9 GHz, (c) 8.5 GHz, and (d) 17.1 GHz.

Fig. 14. P$_D$ over aspect angles curves using measured and simulated AscTec Firefly data for $\overline{SNR}_c = 13$ dB in VV polarization. The plots refer to the frequency bin with central frequency: (a) 14.1 GHz, (b) 15.9 GHz, (c) 8.5 GHz, and (d) 17.1 GHz.
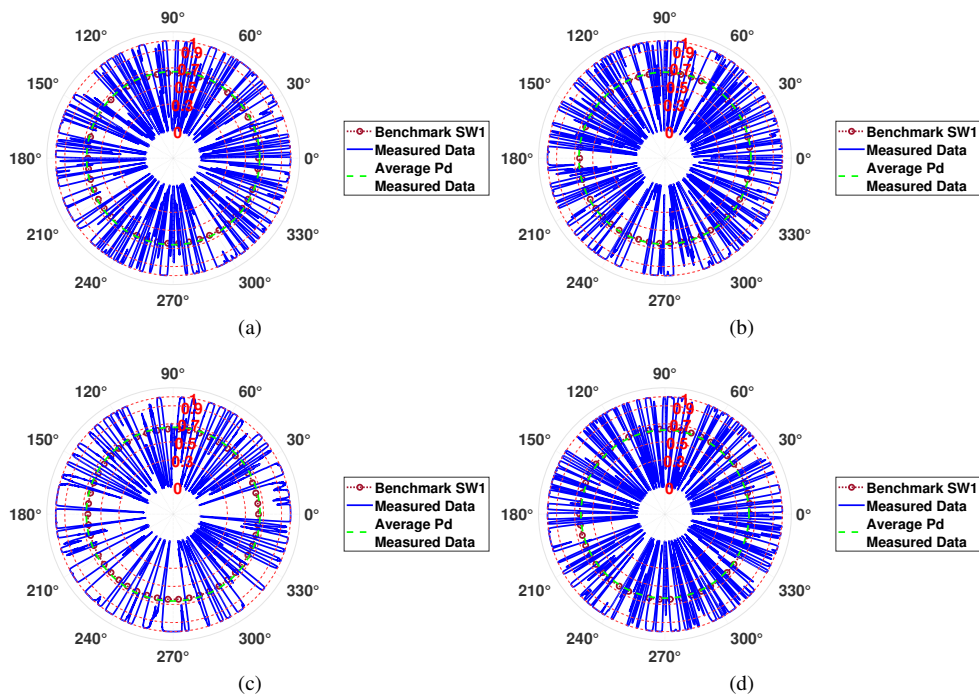
TABLE VII
AVERAGE P$_D$ FOR TWO $\overline{SNR}_c$ VALUES.

	P$_D$ for $\overline{SNR}_c$ = 5 / 13 dB					
Frequency (Pol)	**SW1**	**AscTec Firefly**	**AscTec Pelican**	**Venom VN10**	**Parrot AR.DRONE 2.0**	**DJI Matrice 100**
9 GHz (HH)	0.11/0.64	0.11/0.68	0.12/0.59	0.10/0.72	0.10/0.66	0.11/0.62
9 GHz (VV)	0.11/0.64	0.11/0.67	0.10/0.70	0.11/0.60	0.11/0.67	0.10/0.58
11 GHz (HH)	0.11/0.64	0.10/0.65	0.11/0.62	0.11/0.65	0.11/0.63	0.11/0.65
11 GHz (VV)	0.11/0.64	0.10/0.66	0.11/0.64	0.11/0.63	0.11/0.59	0.10/0.65
13 GHz (HH)	0.11/0.64	0.11/0.66	0.11/0.60	0.11/0.66	0.11/0.68	0.11/0.59
13 GHz (VV)	0.11/0.64	0.10/0.68	0.10/0.67	0.11/0.64	0.11/0.66	0.11/0.65
15 GHz (HH)	0.11/0.64	0.11/0.65	0.11/0.59	0.11/0.65	0.11/0.60	0.10/0.65
15 GHz (VV)	0.11/0.64	0.11/0.62	0.11/0.64	0.11/0.67	0.12/0.59	0.11/0.64
17 GHz (HH)	0.11/0.64	0.11/0.67	0.10/0.56	0.10/0.68	0.10/0.61	0.11/0.63
17 GHz (VV)	0.11/0.64	0.11/0.63	0.10/0.66	0.10/0.70	0.11/0.66	0.10/0.63

TABLE VIII
VALUES OF THE GAMMA SHAPE PARAMETER PERTAINING TO THE CASES
ANALYZED IN FIG. 15.

Drone	**Frequency**	α_{HH}	α_{VV}
Venom VN10	9.1 GHz	1.57	1.08
Parrot AR.DRONE	14 GHz	0.95	1.31
AscTec Pelican	9.2 GHz	0.69	1.27
AscTec Pelican	10.5 GHz	0.86	2.28

[14] A. Balleri, "Measurements of the radar cross section of a nano-drone at K-band," in *2021 IEEE 8th International Workshop on Metrology for AeroSpace (MetroAeroSpace)*, 2021, pp. 283–287.

[15] M. Ritchie, F. Fioranelli, H. Griffiths, and B. Torvik, "Micro-drone RCS analysis," in *2015 IEEE Radar Conference*, 2015, pp. 452–456.

[16] P. J. Speirs, A. Murk, M. Renker, P. Wellig, and U. Aulenbacher, "High-detail simulations of consumer-grade UAV RCS signatures, and comparisons against measurements," *STO-MP-MSG-SET-183*.

[17] P. Sedivy and O. Nemec, "Drone RCS statistical behaviour," *STO-MP-MSG-SET-183*, 2021.

[18] J. Markow, A. Balleri, and A. Catherall, "Statistical analysis of in-flight drone signatures," *IET Radar, Sonar & Navigation*, 2022.

[19] M. Ezuma, C. K. Anjinappa, V. Semkin, and I. Guvenc, "Comparative Analysis of Radar Cross Section Based UAV Classification Techniques," *arXiv preprint arXiv:2112.09774*, 2021.

[20] J. Drozdowicz, M. Wielgo, P. Samczynski, K. Kulpa, J. Krzonkalla, M. Mordzonek, M. Bryl, and Z. Jakielaszek, "35 GHz FMCW drone detection system," in *2016 17th International Radar Symposium (IRS)*, 2016, pp. 1–4.

[21] J. Klare, O. Biallawons, and D. Cerutti-Maori, "Detection of UAVs using the MIMO radar MIRA-CLE Ka," in *Proceedings of EUSAR 2016: 11th European Conference on Synthetic Aperture Radar*, 2016, pp. 1–4.

[22] A. D. de Quevedo, F. I. Urzaiz, J. G. Menoyo, and A. A. López, "Drone detection and radar-cross-section measurements by RAD-DAR," *IET Radar, Sonar & Navigation*, vol. 13, no. 9, pp. 1437–1447, 2019.

[23] F. Hoffmann, M. Ritchie, F. Fioranelli, A. Charlish, and H. Griffiths, "Micro-doppler based detection and tracking of UAVs with multistatic radar," in *2016 IEEE Radar Conference (RadarConf)*, 2016, pp. 1–6.

[24] S. Park and S.-O. Park, "Configuration of an X-band FMCW radar targeted for drone detection," in *2017 International Symposium on Antennas and Propagation (ISAP)*, 2017, pp. 1–2.

[25] M. Caris, W. Johannes, S. Sieger, V. Port, and S. Stanko, "Detection of small UAS with W-band radar," in *2017 18th International Radar Symposium (IRS)*, 2017, pp. 1–6.
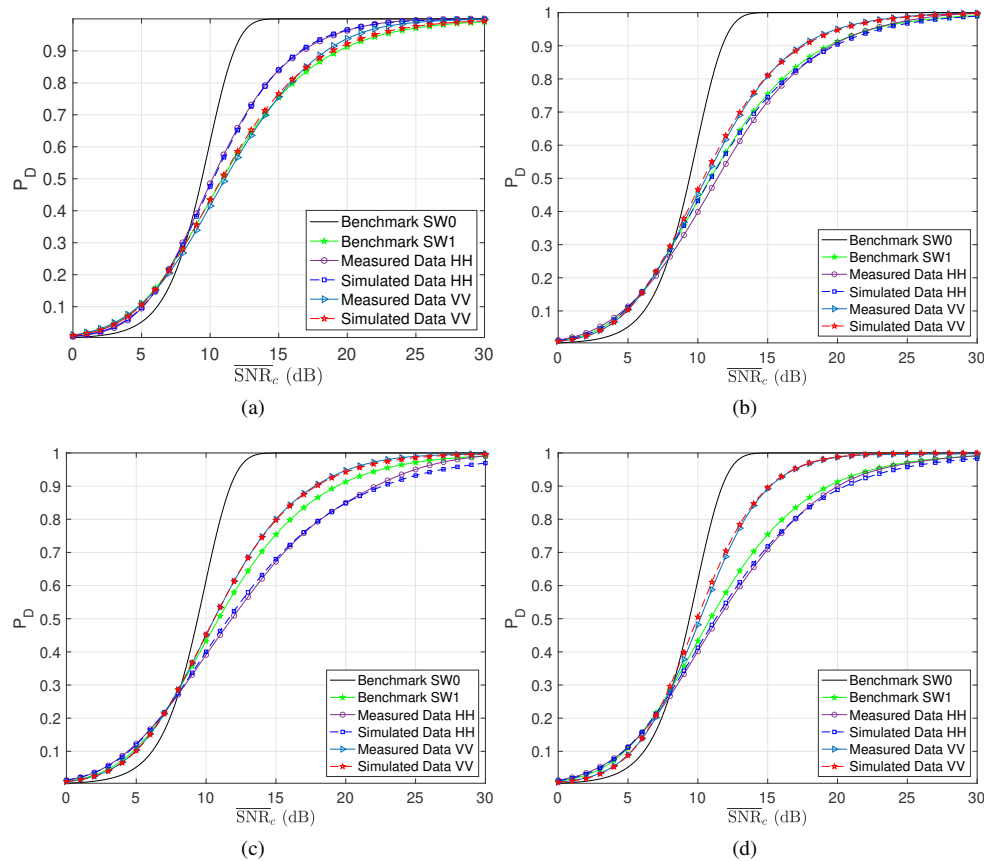
Fig. 15. P_D versus $\overline{\text{SNR}}_c$ for HH and VV polarization curves using measured and simulated drones data: (a) Venom VN10 at 9.1 GHz, (b) Parrot AR.DRONE at 14 GHz, (c) AscTec Pelican at 9.2 GHz, (d) AscTec Pelican at 10.5 GHz.

[26] C. Clemente, F. Fioranelli, F. Colone, and G. Li, *Radar Countermeasures for Unmanned Aerial Vehicles*, IET, London, 2021.

[27] M. A. Richards, J. A. Scheer, and W. A. Holm, *Principles of Modern Radar: Basic Principles, Volume 1*, Institution of Engineering and Technology, 2010.

[28] Calibration and Measurement Guide, *ShockLine MS46122A/B, MS46131A, ME7868A, and MS46322A/B Series Vector Network Analyzer*, Number 10410-00336. Anritsu Company, 2021.

[29] "IEEE recommended practice for radar cross-section test procedures," *IEEE Std 1502-2020 (Revision of IEEE Std 1502-2007)*, pp. 1–78, 2020.

[30] M. F. Sundermeier and D. Fischer, "Compact radar cross-section measurement setup and performance evaluation," *Advances in Radio Science*, vol. 19, pp. 147–152, 2021.

[31] D. E Kerr, *Propagation of short radio waves*, vol. 24, IET, 1987.

[32] E. F. Knott, *Radar cross section measurements*, Springer Science & Business Media, 2012.

[33] C. Hu, N. Li, W. Chen, and L. Zhang, "High-precision RCS measurement of aircraft's weak scattering source," *Chinese Journal of Aeronautics*, vol. 29, no. 3, pp. 772–778, 2016.

[34] D. A. Shnidman, "Expanded swerling target models," *IEEE Trans. Aerosp. Electron. Syst.*, vol. 39, no. 3, pp. 1059–1069, 2003.

[35] A. De Maio, A. Farina, and G. Foglia, "Target fluctuation models and their application to radar performance prediction," *IEE Proceedings-Radar, Sonar and Navigation*, vol. 151, no. 5, pp. 261–269, 2004.

[36] R. D'Agostino and M. Stephens, *Goodness-of-Fit Techniques*, New York: Marcel Dekker, 1986.

[37] J. A. Nelder and R. Mead, "A simplex method for function minimization," *The computer journal*, vol. 7, no. 4, pp. 308–313, 1965.

[38] W. W. Daniel, *Applied Nonparametric Statistics*, Duxbury advanced series in statistics and decision sciences. PWS-KENT Pub., 1990.

[39] S. A. Teukolsky W. H. Press, B. P. Flannery and W.T. Vetterling, *Numerical recipes in C: The art of scientific computing*, MA: Cambridge University Press, Cambridge, 1997.

[40] R. Simard and P. L'Ecuyer, "Computing the two-sided kolmogorov-smirnov distribution," *Journal of Statistical Software*, vol. 39, pp. 1–18, 2011.

[41] M. B. Wilk and R. Gnanadesikan, "Probability plotting methods for the analysis for the analysis of data," *Biometrika*, vol. 55, no. 1, pp. 1–17, 1968.

[42] H. Thode, *Testing for normality*, Marcel Dekker, New York, 2002.

[43] E. F. Knott, J. F. Schaeffer, and M. T. Tulley, *Radar Cross Section*, Radar, Sonar and Navigation. Institution of Engineering and Technology, 2004.

[44] D. P. Meyer and H. A. Mayer, "Radar target detection- handbook of theory and practice," *New York, Academic Press, Inc., 1973. 508 p*, 1973.

[45] P. Swerling, "Probability of detection for fluctuating targets," *IRE Transactions on Information Theory*, vol. 6, no. 2, pp. 269–308, 1960.

[46] J. Marcum, "A statistical theory of target detection by pulsed radar," *IRE Transactions on Information Theory*, vol. 6, no. 2, pp. 59–267, 1960.

Massimo Rosamilia (S'20) received the B.S. (with honors) and M.S. degrees in computer engineering from the University of Salerno, Fisciano, Italy, in 2017 and 2019, respectively. From September to November 2021, he was a Visiting Ph.D Student with the Cranfield University, Shrivenham, U.K. From September to December 2022, he was a Visiting Ph.D Student with the University of Luxembourg, Luxembourg. He is currently working toward the Ph.D. degree in information technologies and electrical engineering with the University of Naples Federico II, Naples, Italy. His research interest lies in the field of statistical signal processing, with emphasis on radar signal processing. He ranked second in the Student Contest of the 1st International Virtual School on Radar Signal Processing, in 2020, with the contribution "Simultaneous Radar Detection and Constrained Target Angle Estimation via Dinkelbach Algorithm".

Alessio Balleri received the Laurea degree in telecommunication engineering (summa cum laude) (five legal years) from the University of Pisa, Italy, in 2004, and the Ph.D. degree in electronic and electrical engineering from the University College London (UCL), London, U.K., in 2010. From February 2010 to March 2012, he was a Research Associate in radar systems with the Department of Electronic and Electrical Engineering, UCL. From June 2004 to December 2004, he was a Visiting Research Scholar with the Department of Electrical and Computer Engineering, University of Illinois at Chicago. He is currently a Reader in radar systems with Cranfield University, Shrivenham, U.K. His research interests include radar and sonar system design, biologically inspired radar and sonar systems, adaptive radar, radar and sonar target classification, target feature extraction, and modeling of radar clutter. Dr. Balleri Guest Coedited a special issue on "Biologically Inspired Radar and Sonar Systems" for the IET Radar, Sonar and Navigation in 2012 and a special issue on "Emerging Radar Techniques" for the EURASIP Journal on Advances in Signal Processing, in 2013. He was the Technical Program Committee Co-Chair for the IET International Radar Conference 2017, Belfast, U.K. and the Technical Co-Chair of the 2020 IEEE International Radar Conference, Washington, DC, USA. He is currently serving as the Special Issue editor for the IET Radar, Sonar & Navigation journal and he has recently been elected as a member of the IEEE AESS Radar System Panel.

Vincenzo Carotenuto (S'12-M'16-SM'19) received the M.Sc. degree in telecommunication engineering and the Ph.D. degree in electronic and telecommunication engineering from the University of Naples Federico II, Naples, Italy, in 2010 and 2015, respectively. He is currently under research agreement with the Department of Electrical and Information Technology Engineering, University of Naples Federico II. His research interest lies in the field of statistical signal processing, with an emphasis on radar signal processing. He is also the co-recipient of the 2018 IEEE International Workshop on Metrology for Aerospace Best Radar Paper Award with the contribution "Assessing Spectral Compatibility Between Radar and Communication Systems on Measured Data".
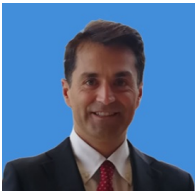
Antonio De Maio (S'01-A'02-M'03-SM'07-F'13) received the Dr. Eng. (Hons.) and Ph.D. degrees in information engineering from the University of Naples Federico II, Naples, Italy, in 1998 and 2002, respectively. From October to December 2004, he was a Visiting Researcher with the U.S. Air Force Research Laboratory, Rome, NY, USA. From November to December 2007, he was a Visiting Researcher with the Chinese University of Hong Kong, Hong Kong. He is currently a Professor with the University of Naples Federico II. His research interest lies in the field of statistical signal processing, with emphasis on radar detection, optimization theory applied to radar signal processing, and multiple-access communications. He is the recipient of the 2010 IEEE Fred Nathanson Memorial Award as the young (less than 40 years of age) AESS Radar Engineer 2010 whose performance is particularly noteworthy as evidenced by contributions to the radar art over a period of several years, with the following citation for "robust CFAR detection, knowledge-based radar signal processing, and waveform design and diversity". He is the corecipient of the 2013 best paper award (entitled to B. Carlton) of the IEEE Transactions on Aerospace and Electronic Systems with the contribution "Knowledge-Aided (Potentially Cognitive) Transmit Signal and Receive Filter Design in Signal-Dependent Clutter".

Augusto Aubry (M'12-SM'16) received the Dr. Eng. degree in telecommunication engineering (with honors) and the Ph.D. degree in electronic and telecommunication engineering both from the University of Naples Federico II, Naples, Italy, in 2007 and 2011, respectively. From February to April 2012, he was a Visiting Researcher with the Hong Kong Baptist University, Hong Kong. He is currently an assistant Professor with the University of Naples Federico II. His research interests include statistical signal processing and optimization theory, with emphasis on MIMO communications and radar signal processing. He is also the co-recipient of the 2013 Best Paper Award (entitled to B. Carlton) of the IEEE Transactions on Aerospace and Electronic Systems with the contribution "Knowledge-Aided (Potentially Cognitive) Transmit Signal and Receive Filter Design in Signal-Dependent Clutter". Dr. Aubry was the Recipient of the 2022 IEEE Fred Nathanson Memorial Award as the young (less than 40 years of age) AESS Radar Engineer 2022, with the following citation "For outstanding contributions to the application of modern optimization theory to radar waveform design and adaptive signal processing".